

Hierarchical MOF-xerogel monolith composites from embedding MIL-100(Fe,Cr) and MIL-101(Cr) in resorcinol-formaldehyde xerogels for water adsorption applications

Martin Wickenheisser ^a, Annika Herbst ^a, René Tannert ^b, Barbara Milow ^b, Christoph Janiak ^{a,*}

^a *Institut für Anorganische Chemie und Strukturchemie I, Universitätsstraße 1, 40225 Düsseldorf, Germany. E-mail: janiak@uni-duesseldorf.de*

^b *Deutsches Zentrum für Luft- und Raumfahrt (DLR), Institut für Werkstoff-Forschung, Aerogele, Linder Höhe, 51147 Köln, Germany*

Abstract

Shaping of otherwise powdery metal-organic frameworks is recognized as a more-and-more important issue to advance them to the application stage. Monolithic MOF composites were synthesized using micro-to-mesoporous MIL-100(Fe,Cr) and MIL-101(Cr) as thermally and chemically stable MOFs together with a mesoporous resorcinol-formaldehyde based xerogel as binding agent. The monolithic bodies could be loaded with up to 77 wt% of powdery MIL material under retention of the MIL surface area and porosities (from N₂ adsorption) by pre-polymerization of the xerogel solution. The obtained monoliths are mechanically stable and adsorb close to the expected water vapor amount according to the MIL weight percentage. There is no loss of BET surface area, porosity and water uptake capacity especially for the MIL-101(Cr) composites. Water vapor adsorption isotherms show that the 77 wt% MIL-101(Cr) loaded composite even features a slightly increased water vapor uptake compared to pure MIL-101(Cr) up to a relative vapor pressure of $P \cdot P_0^{-1} = 0.5$. These hydrophilic monolithic composites could be applied for heat transformation application such as thermally driven adsorption chillers or adsorption heat pumps.

Keywords: Metal-organic framework, Resorcinol-formaldehyde xerogels, Monoliths, Water adsorption, Heat transformation.

1. Introduction

MOFs (metal-organic framework) are potentially porous coordination networks based on metal ions or metal clusters, connected by organic ligands [1]. Metal organic frameworks are often three-dimensional networks and have uniform micropore structures with high surface areas and large pore volumes. Research tries to advance MOFs towards applications [2,3], such as catalysis [4,5,6], gas storage [7,8,9] and gas separation [10,11,12,13]. Many review articles are evidence to the increasing interest in MOF chemistry over the last years [14,15,16,17,18].

Recently, MOFs are investigated as microporous materials for cycling water sorption for heat transformation: During hot seasons in large part of cities energy consumption caused by electric air-conditioning represents 30 to 50 % of total electric energy consumed [19]. Therefore it would be beneficial to use a cooling system based on adsorption chilling running on solar thermal energy. In this context sorption-based heat transformations attracted growing interest during the last years [20,21,22,23].

A schematic diagram of a thermally driven adsorption chiller or adsorption heat pump is depicted in Figure 1. Bed 1 and Bed 2 contain the porous (MOF-) material in combination with a heat exchange device and are switched between the working and regeneration cycle. During the working cycle, adsorption of the working fluid (e.g. water) takes place in the bed until the desired loading is reached. At the same time the other bed is regenerated by applying heat to desorb the working fluid. The desorbed vapor is liquefied in the condenser and the liquid working fluid then flows back to the evaporator, where again evaporation takes place. The heat of condensation (Q_{out}^{cond}) and the heat of adsorption (Q_{out}^{ads}) can be used in a heating application or are dissipated to the environment. From the heat of evaporation (Q_{in}^{evap}) either useful cold is generated for the cooling application or it is the low-temperature

heat (blue) which is converted to medium temperature levels (green) by means of the driving heat of desorption $Q_{in}^{drive,des}$ (red). When the water loadings in bed 1 and 2 reach the same level, the two beds are interchanged with respect to regeneration and working cycle by closing and opening the respective valves [24].

Figure 1.

The key part of the system is the sorption material which should have a high water loading lift in the ideal interval $0.05 < P \cdot P_0^{-1} < 0.35$. Water is the working fluid of choice because of its high evaporation enthalpy ($2440 \text{ kJ} \cdot \text{kg}^{-1}$ at $25 \text{ }^\circ\text{C}$) and non-toxicity despite the need to work under vacuum because of the low vapor pressure of only 3.17 kPa at $25 \text{ }^\circ\text{C}$ [15,25,26]. During the last years significant progress has been made in the development of MOF-based sorption materials [27]. Various materials, predominately of the MIL (Materials of Institute Lavoisier) family, have been investigated for water adsorption [28,29] and also different strategies of tuning prototypical MOFs to enhance the water uptake have been examined [30,31]. Long term and cycle measurements have been performed to ensure the required water stability [32,33,34]. Three of these MOFs, namely MIL-100(Fe,Cr) and MIL-101(Cr), were selected for the present study due their good water sorption properties and stability [31,35].

MIL-100 $\{M_3(\mu_3\text{-O})(X)(\text{H}_2\text{O})_2(\text{BTC})_2 \cdot n\text{H}_2\text{O}\}_n$ ($M = \text{Cr}$ [36,37], Fe [38,39,40,41]; $X = \text{OH}, \text{F}$; $\text{BTC} = 1,3,5\text{-benzene tricarboxylate}$) possesses two types of mesopores with cages of 25 \AA and 29 \AA in diameter consisting of hexagonal (8.6 \AA) and pentagonal windows ($4.7\text{--}5.5 \text{ \AA}$) (Fig. A.17, Fig. 2) [38]. MIL-101(Cr) [42] $\{\text{Cr}_3(\mu_3\text{-O})(\text{F},\text{OH})(\text{H}_2\text{O})_2(\text{BDC})_3 \cdot \sim 25\text{H}_2\text{O}\}_n$ is a micro- and mesoporous material, having 1,4-benzene dicarboxylate (BDC) as linker, with hexagonal ($15\text{--}16 \text{ \AA}$) and pentagonal windows (12 \AA) and inner free cages of 29 \AA and 34 \AA in diameter (Fig. A.16, Fig. 2). The water uptake of MIL-100(Cr), MIL-100(Fe) and MIL-101(Cr) are in the range of $0.6\text{--}0.7 \text{ g g}^{-1}$, $0.65\text{--}0.75 \text{ g g}^{-1}$ and $1.0\text{--}1.5 \text{ g g}^{-1}$, respectively [33].

Figure 2.

MOFs are typically obtained as crystalline fine powders, yet almost every application requires an appropriate shaping, *e.g.*, monolithic structures, of the used materials without diminishing its useful properties [43,44].

Different strategies of shaping MOFs have been investigated so far [43,45,46]: One possibility is to press the material into tablets or pellets [47]. MOF-177 has been mechanically compressed to a monolithic structure, resulting in enhanced hydrogen storage capacity, but also leading to an amorphous material [48]. An alternative strategy is the preparation of pure MOF monoliths, although there are often difficulties in obtaining phase pure MOFs and retaining porosity [49]. More studies have been performed on MOF composites where an organic or inorganic additive acts as binder to shape the material [17,50,51,52,53]. The resulting monoliths or membranes were tested for example in separation processes [54,55].

Aerogels are characterized by high porosity and high surface area as well as a low density and low thermal conductivity [56,57]. To obtain an aerogel with these properties supercritical drying with CO₂ is a necessary step [56,58]. Resorcinol-formaldehyde based gels can be dried under atmospheric conditions, if the ratio of resorcinol to basic catalyst is high enough leading to mechanically stable xerogels with negligible shrinking during the drying procedure [59]. In the following, the term xerogel is defined as subcritically dried and aerogel is used for supercritical dried materials. Easily obtainable resorcinol-formaldehyde aero- and xerogels are well investigated and can be tuned by several parameters. For example, the ratio of resorcinol and catalyst as well as the pH of the solution influences the properties of the gel material [60,61,62]. A major advantage, in terms of embedding porous materials, is the possibility of pre-polymerizing the polymer, which was reported first by Czakkel et al. [63]. By applying this method to MOF polymer composites, pore-blocking effects, which often occur in composite syntheses, could be avoided in order to retain the porous properties of the MOFs [43,45,53].

In this work, we present for the first time the embedding of three different metal-organic frameworks (MIL-100(Fe, Cr) and MIL-101(Cr)) in resorcinol-formaldehyde xerogels and investigate the resulting monoliths for their porosity and water-sorption behavior.

2. Experimental section

2.1 Materials and methods

All chemicals were obtained commercially and were used without further purification: Fe⁰ powder (Riedel-de Haën, > 99 %), CrO₃ (Alfa Aesar, 99 %), Cr(NO₃)₃·9H₂O (Acros Organics, 99 %), hydrofluoric acid (Acros Organics, 48-51 wt% in H₂O), HNO₃ (Grüssing, 65 wt%), 1,3,5-benzenetricarboxylic acid (H₃BTC) (Alfa Aesar, 98 %), 1,4-benzenedicarboxylic acid (H₂BDC) (Acros Organics, > 99 %), tetramethylammonium hydroxide (TMAOH) (Alfa Aesar, 25 wt% in water), resorcinol (Acros Organics, 98 %), Na₂CO₃ (Riedel-de Haën, > 99.8 %), formaldehyde (VWR, 24 wt% in water), acetic acid (VWR, 99.9 %), DMF (VWR, p.a.), ethanol (VWR, p.a.). All experimental work was performed in air.

2.2 Physical measurements

Powder X-ray diffraction (PXRD) diffractograms were obtained at ambient temperature on a Bruker D2 Phaser with a flat sample holder using Cu-K α radiation ($\lambda = 1.54182 \text{ \AA}$). Fourier transform infrared spectra were done on a Bruker TENSOR 37 IR spectrometer at ambient temperature in a KBr disk in a range of 4000 to 500 cm⁻¹. Nitrogen physisorption isotherms were carried out on a Nova 4000e from Quantachrome at 77 K. Water physisorption isotherms were measured volumetrically on a Quantachrome Autosorb iQ MP at 293 K. For measuring the isotherms the materials were loaded into glass tubes capped with septa. The weighted tubes were attached to the corresponding degassing port of the sorption analyzer, degased under vacuum at elevated temperature, weighted out again and then transferred to the analysis port of the sorption analyzer. BET surface areas were calculated from the

nitrogen physisorption isotherms. DFT calculations for the pore size distribution curves were done with the native NovaWin 11.03 software using the 'N₂ at 77 K on carbon, slit pore, nonlinear density functional theory (NLDFT) equilibrium' model [64,65,66]. Scanning electron microscopic images were done on a LEO 1430 VP (native xerogel, MIL-100(Fe)@xerogel), on a LEO 982 (77 wt%, MIL-101(Cr)@xerogel-H₂O) both from Zeiss and on a JSM-6510 (MIL-100(Cr)@xerogel; 35 wt%, MIL-101(Cr)@xerogel) from Jeol. The samples were coated with Au for 180 sec at 30 mA by an AGAR sputter coater (LEO 1430 VP), sputtered with chromium (approx. 10 nm thickness, LEO 982) or with Au for 20 sec at 35 mA by an Jeol JFC-1200 sputter (JSM-6510). The thermogravimetric analysis (TGA) curve of native R,F-xerogel was measured on a TG 209 F3 Tarsus from Netzsch in the temperature range between 303 and 873 K, with heating rate of 3 K·min⁻¹.

2.3 Synthesis of MIL-100(Fe,Cr) and MIL-101(Cr)

MIL-100(Fe), MIL-100(Cr) and MIL-101(Cr) were hydrothermally synthesized according to the literature [67,68,69]. Typical batch sizes of 665 mg Fe⁰ powder (11.9 mmol), 1.65 g H₃BTC (7.85 mmol), 0.83 mL hydrofluoric acid (24 mmol; 48-51 wt% in H₂O), 0.5 mL HNO₃ (7 mmol; 65 wt%) and 60 mL of deionized H₂O (for *MIL-100(Fe)*), 1.20 g CrO₃ (12.0 mmol), 2.52 g H₃BTC (12.0 mmol), 0.42 mL hydrofluoric acid (12 mmol; 48-51 wt% in H₂O) and 58 mL of deionized H₂O (for *MIL-100(Cr)*) and 4.80 g (12.0 mmol) Cr(NO₃)₃·9H₂O, 1.98 g (11.9 mmol) H₂BDC, 1.1 mL TMAOH (3.1 mmol; ρ = 1.014 g·mL⁻¹; 25 wt% in H₂O) and 60 mL of deionized water (for *MIL-101(Cr)*) yielded the raw MILs. For further activation the MILs were purified through a consecutive washing procedure with DMF, EtOH and deionized water (see supplementary data for details). 1.50, 3.18 and 2.34 g of purified MIL-100(Fe), MIL-100(Cr) and MIL-101(Cr) were isolated (41, 69 and 50 % yield based on Fe or Cr), as orange-brown (MIL-100(Fe)) and green powders (MIL-100/101(Cr)) with BET surface areas and pore volumes shown in Table 1. Pore volumes (measured at P/P₀⁻¹ = 0.95) and BET surface areas were calculated from the type I N₂ sorption isotherms (Fig. A.2a, A.4a, A.6a, Table 1).

Experimental, theoretical powder X-ray patterns and the IR-spectra are shown in Fig. A.1, A.3, A.5.

2.4 Synthesis of native R,F-xerogel

The polycondensation reaction of resorcinol and formaldehyde is initiated by the basic catalyst Na_2CO_3 , which first leads to deprotonation of the acidic phenol groups followed by addition of formaldehyde to the phenol ring. The formed hydroxymethyl functionalities ($-\text{CH}_2\text{OH}$) undergo a condensation reaction forming a methylene ($-\text{CH}_2-$)- and methylene ether ($-\text{CH}_2\text{OCH}_2-$)-bridged polymer illustrated in Scheme 1. For gelation (polymerization) typically resorcinol (R) and formaldehyde (F) are dissolved in a basic, aqueous Na_2CO_3 solution (C, $c = 2.1 \cdot 10^{-3} \text{ mol} \cdot \text{L}^{-1}$). The base C is essential for the formation of the R anions, which are more active towards the addition of F compared to uncharged, neutral R. After a short period of stirring (5 min), the so-called sol mixture, is transferred into an appropriate mold and cured for 7 days at 333 K. The curing of the sol leads to a monolithic product, which is then placed for 1 day in dilute acetic acid solution to increase the crosslinking of the residual hydroxymethyl groups. The monolithic resorcinol-formaldehyde polymers are washed in ethanol several times and finally dried subcritically by conventional evaporation of the solvent at atmospheric pressure (see supplementary data for details). The obtained brown-colored polymers are called “xerogels”. Supercritical drying with CO_2 would lead to so-called “aerogels”. The choice of the catalyst concentration, the initial gel pH, the concentration of R and F in the sol, dilution effects and the way of drying the monoliths all influence the particle size, density, surface area and mechanical strength of the final monoliths. For a detailed analysis of these factors the reader is referred to other literature [56,60,61].

Scheme 1.

2.5 Syntheses of MIL-100(Fe,Cr)@xerogel and MIL-101(Cr)@xerogel

MIL@xerogel with different wt% of MILs were synthesized by homogenization of the MIL powders with the pre-polymerized R,F-xerogel solution. The prepared R,F-xerogel solution was filled into syringes (approx. 1 g per syringe), which were cut off from the cannula side, properly sealed by several layers of polyethylene- and aluminum foil and pre-polymerized for 5 h at 343 K. During this step the native R,F-xerogel changed from a clear, almost colorless solution to a honey-like, viscous material (Fig. A.11). Various amounts of well-ground MIL-100(Fe), MIL-100(Cr) and MIL-101(Cr) powders (100, 150 and 180 mg) were added to the pre-polymerized R,F-xerogel. After homogenization of the mixtures directly in the syringes by a spatula, curing, washing and drying brown monoliths with MIL contents between 35 and 58 wt% were isolated. To maximize the amount of MOF powder in the composites, one MIL-101(Cr)@xerogel-H₂O with 77 wt% of MIL was synthesized by additional usage of water to the pre-polymerized xerogel for proper homogenization of the MIL@xerogel mixture yielding a green monolith (Fig. 3). The suffix -H₂O is added to MIL@xerogel, when additional water was used in the composite syntheses. MIL-101(Cr)@xerogel-H₂O (35, 46, 50 wt%) were also obtained using additional water during the synthetic procedure (see supplementary data for details). If no additional water was used, the term 'standard synthesis' was used.

Figure 3.

3. Results and discussion

3.1 Native R,F-xerogel

Infrared data (Fig. 4a) of the native or bulk resorcinol-formaldehyde based xerogel reveal the expected organic functional groups (*cf.* R,F-xerogel structure in Scheme 1). The broad band between 3700 and 3000 cm⁻¹ is associated with the $\nu(\text{O-H})$ stretching vibrations, originating

from the phenol groups and water molecules in the hydrophilic xerogel. Aliphatic stretching vibrations $\nu(\text{CH}_2)$ can be assigned to the band at 2931 cm^{-1} . The corresponding $\delta(\text{CH}_2)$ deformation vibration is located at 1474 cm^{-1} . The band at 1613 cm^{-1} corresponds to the aromatic ring stretching vibration $\nu(\text{C}=\text{C})$ and valence vibration bands at 1217 and 1092 cm^{-1} reveal the presence of the methylene ether bridges $\nu(\text{C}-\text{O}-\text{C})$. The IR-spectrum is consistent with other literature data [70].

The porous nature of the xerogel is verified by N_2 sorption experiments (Fig. 4b). The N_2 sorption isotherm exhibits a mixture of type II (macroporous) shape together with type IV (mesoporous) shape, due to the hysteresis between adsorption and desorption isotherm [71]. The pore volume of $0.16\text{ cm}^3\cdot\text{g}^{-1}$ and the BET surface area of $100\text{ m}^2\cdot\text{g}^{-1}$, both calculated from the N_2 adsorption isotherm, are typical values for subcritically dried R,F-xerogels with the following molar ratios of the starting materials: resorcinol/formaldehyde = 0.73, resorcinol/ Na_2CO_3 = 1000, resorcinol/water = 0.031 (Table 1) [60,70,72].

Scanning electron microscopy (SEM) images displays the typical morphological surface known for resorcinol-formaldehyde xerogels with low catalytic Na_2CO_3 concentrations (high resorcinol/ Na_2CO_3 molar ratios of R/C = 1000) (Fig. 4c). The morphology can be described as interconnected colloidal-like particles, which do not possess porosity themselves, but generate porosity between the gaps of the particles [60,70].

Thermogravimetric analysis of the native xerogel shows a first mass loss of approximately 10 wt% up to temperature of 473 K, which can be assigned to the loss of physisorbed water (Fig. A.7a). The R,F-xerogel is thermally stable up to 493 K. The first mass loss of 10 wt% of water together with the shape of its water adsorption isotherm, showing an almost linear rise of water vapor with a total water uptake of $0.10\text{ g}\cdot\text{g}^{-1}$ at $P\cdot P_0^{-1} = 0.9$, indicates a hydrophilic character, which is comparable to silica gels (Fig. 4d, Table 1).

Figure 4.

3.2 Embedding MIL-100(Fe,Cr) and MIL-101(Cr) into R,F-xerogel monoliths

Monolithic composites, consisting of a metal-organic framework (e.g. MILs) and an organic polymer (e.g. R,F-xerogel), can be synthesized in two different ways: (i) The synthesized MIL powder can either be mixed together with the just prepared xerogel solution, followed by curing, washing and drying steps ('direct route'). (ii) The MIL can be synthesized *in situ* into the already cured, porous system of a R,F-xerogel monolith by impregnating it with the corresponding starting materials (metal source and linker) followed by an appropriate temperature program ('in-situ route'). Through the direct route the ratio of MIL and R,F-xerogel in the final monolithic product can easily be predetermined by varying the amount of MIL powder and xerogel solution, which is not that realizable in the in-situ route. A disadvantage of the direct route is that the micro- and mesopores of the MOF can be blocked by the monomers or oligomers of the xerogel precursors. This pore blocking is accompanied by a pronounced decrease of the total surface area of the monolith. In this paper, we describe how to avoid pore blocking by pre-polymerization of the xerogel solution, resulting in highly porous and therefore active monolithic MIL@xerogel composites through the direct route.

In a first experiment aimed to synthesize a highly porous composite, MIL-100(Cr) powder was mixed together with an excess of the just prepared R,F-xerogel solution without any pre-polymerization. To maximize the amount of MIL in the monolithic composite, the powder was sedimented for one day followed by curing. After washing and drying steps the resulting monolith consisted of a brown bottom layer containing MIL and xerogel and a top brown layer, which represents the pure xerogel (Fig. A.8a). Powder X-ray diffraction pattern and infrared spectrum reveal the unchanged presence of the MIL-100(Cr) phase in the composite material (Fig. A.8b-c), but the N₂-sorption isotherm and the corresponding pore size distribution curve showed only a small residual porosity of 20 m²·g⁻¹, indicative of complete

blockade of the micro- and mesopores of MIL-100(Cr) in the monolithic composite (Fig. A.9a-b) (see supplementary data for details). The disappearance of the MIL pores in the composites occurs through the initial filling of the micro- and mesopores or at least the pore mouths by resorcinol and formaldehyde molecules followed by polycondensation inside these MIL pores or pore mouths.

For the synthesis of highly porous monolithic MOF@xerogel composites the MIL pores have to be protected during the synthesis. To avoid, or at least minimize polymerization reactions of resorcinol and formaldehyde inside the MIL pores, the xerogel solution has to be pre-polymerized before adding the MIL powder to create larger resorcinol-formaldehyde oligomers or small polymer strands. Those larger oligomers should be less prone to diffuse into and block the MIL pores.

Similar experiments were carried out here on MIL-100(Fe)@xerogel composites. Identical amounts of just prepared xerogel solution were placed for 3, 4 and 5 h into an oven at 343 K. After 3, 4 and 5 h of pre-polymerization time the viscous solutions were mixed together with 100 mg of MIL-100(Fe) powder, respectively. Homogenization, curing, washing and drying were done according to the native R,F-xerogel synthesis yielding brown monoliths each with 11 wt% of MIL-100(Fe) (see supplementary data for details). X-ray diffraction patterns and infrared spectra prove the existence of MIL-100(Fe) in all three composites (Fig. A.12a-b). The weight-averaged estimated BET surface area of the composite would be $= \frac{\text{wt\% of xerogel}}{100} \times 100 \text{ m}^2 \cdot \text{g}^{-1} + \frac{\text{wt\% of MIL}}{100} \times 2200 \text{ (MIL - 100Fe) m}^2 \cdot \text{g}^{-1}$. For 11 wt% of MIL-100(Fe) the estimated BET surface of the composite would then be $\sim 330 \text{ m}^2 \cdot \text{g}^{-1}$. The corresponding N₂-sorption isotherms yield increased BET surface areas by elongation of the pre-polymerization time of the xerogel solution: $180 \text{ m}^2 \cdot \text{g}^{-1}$ for 3 h, $210 \text{ m}^2 \cdot \text{g}^{-1}$ for 4 h, $220 \text{ m}^2 \cdot \text{g}^{-1}$ for 5 h (Fig. 5a). Pore size distribution curves also confirm the increasing fraction of the MIL-100(Fe) micropores with elongation the pre-polymerization rate (Fig. 5b). After 3 h the MIL-100(Fe) pores between 12–21 Å are hardly visible in the composite material,

whereas 4 and 5 h of pre-polymerization time leads to more accessible, clearly observable micropores.

Figure 5.

The pre-polymerization rate is not only controllable by temperature and time. Also the amount of xerogel solution at a given concentration is an important parameter. A larger amount of a xerogel solution needs more time for curing at a given temperature. It has been found that the maximum pre-polymerization time for 1 g of xerogel solution at 343 K is 5 h. With a longer temperature treatment the MIL powder and pre-polymerized xerogel solution cannot be homogenized properly any more.

Different, mechanically stable, monolithic MIL@xerogel composite materials were synthesized using well-ground MIL-100(Fe), MIL-100(Cr) and MIL-101(Cr) powder (100–460 mg) respectively and 1 g of pre-polymerized (5 h, 343 K) xerogel solution for each monolith. Figure 3 shows the pure R,F-xerogel monolith together with MIL-100(Fe)@xerogel (43 wt%), MIL-100(Cr)@xerogel (41 wt%) MIL-101(Cr)@xerogel (50 wt%) and MIL-101(Cr)@xerogel-H₂O (77 wt%) (from left to right). To maximize the amount of MOF in the composite, a small amount of water was added to the pre-polymerized xerogel to reach a proper homogenization with 77 wt% MIL-101(Cr) in the composite material (see supplementary data for details). Increasing the amount of MIL-101(Cr) powder up to 77 wt% yielded green monolith with the typical green color of MIL-101(Cr). Other monolithic composites using lower weight percentages of orange-brown MIL-100(Fe) or green MIL-100/101(Cr) powders yielded brown monoliths. Mechanical stability tests have been carried out on the pure R,F-xerogel and three representative composites in a shaking incubator for 3 hours to determine the abrasion under mechanical treatment (see supplementary data for details, Fig. A.18). Pure R,F-xerogel shows the lowest degree of abrasion with only 1.1 wt% of mass loss. The

composites feature more abrasion (6.8–19.5 wt% mass loss) due to the MIL content, but fortunately none of the tested monoliths did break into granules through shaking for 3 hours.

Representative scanning electron microscopy images of MIL-100(Fe)@xerogel (43 wt%) and MIL-101(Cr)@xerogel-H₂O (77 wt%) (Fig. 6a-d) show the typical octahedral MIL morphologies with particle sizes between 2–5 μm for MIL-100(Fe) and 300–500 nm for MIL-101(Cr) in the composites [69,73]. MIL octahedrons and xerogel substrate are well grown together to a physical mixture with the xerogel surrounding the MIL particles and with both components showing a reasonable adherence (Fig. 6). The increasing amount of MIL octahedrons in the composites is obvious by comparing Figure 6a-b (43 wt% MIL) with Figure 6c-d (77 wt% MIL). The embedding of MOF particles leads to a high dispersion of MIL crystallites in the xerogel matrix.

Figure 6.

Powder X-ray diffraction patterns of MIL@xerogel compounds demonstrate the unchanged, crystalline phase of the respective MILs in the composites (Fig. A.19a-c) although the reflections of MIL-101(Cr) composites are slightly broadened compared to bulk MIL-101.

Infrared spectra of the composite materials represent an additive overlap of the individual spectra of the corresponding components (MILs and xerogel) (Fig. A.20a-c). With increasing loading of MIL in the MIL@xerogel composites, the intensities of bands, coming from the MIL components are enhanced. The regions highlighted by square brackets in Figure A.20 show the increasing bands for the asymmetric [$\nu_{as}(\text{R-CO}_2)$, region 1] and symmetric [$\nu_s(\text{R-CO}_2)$, region 2] valence-vibrations of the coordinated BDC- or BTC-ligand of the MILs. Region 3 displays the deformation-vibration of the carboxyl groups [$\delta(\text{R-CO}_2)$].

3.3 N₂- and water sorption studies

N₂ sorption measurements have been carried out for all pre-polymerized MIL@xerogel composites (Fig. 7a, c, e). The nitrogen adsorption capacities increase continuously with increasing the MIL content. The composites feature a transition from type II/IV for the bulk R,F-xerogel to type I shaped N₂ isotherms with the MIL additive and its free and accessible micropores. The steep rise at low relative pressures, typical for type I isotherms, becomes more pronounced with increasing MIL ratios. BET surface areas increase with the amount of MIL in the monolithic composites (Table 1). The relevant comparison is to the estimated mass-weighted surface areas of bulk MIL and xerogel using Formula (I) from Table 1. MIL-100(M)@xerogel (M = Fe, Cr) composites reach approximately 60 % of the estimated surface areas. MIL-101(Cr)@xerogel composites with MIL loading between 35 and 50 wt% achieve nearly 83 % of the expected values. The higher BET surface areas for MIL-101 composites, compared to the MIL-100 composites, can be explained by pronounced pore blocking effects in the MIL-100 containing composites. The xerogel binding agent can more easily diffuse and therefore block the smaller MIL-100 pores due to the smaller windows size of MIL-100 (4.7–5.5 Å, 8.6 Å) compared to the windows of MIL-101 (12 Å, 15–16 Å) (Fig. A.16, Fig. A.17, Fig. 2). In other words: Smaller pores are more difficult to protect than larger pores.

Figure 7.

As stated above, to maximize the amount of MIL-101(Cr) in the monolithic composite a small amount of additional water was added to the pre-polymerized xerogel solution together with MIL-101 powder to achieve a proper homogenized mixture (see supplementary data for details). The resulting monolith with 77 wt% of MIL-101(Cr) shows a BET surface which is even slightly higher (+150 m²·g⁻¹) than the estimated BET (Table 1). The addition of water with the MIL could lead to formation of a water layer around the MIL crystallites; thereby prevent pore blocking by the xerogel. This assumption is supported by comparison of

the SEM images of 35 wt% MIL-101(Cr)@xerogel-H₂O (Fig. A.15) and 35 wt% MIL-101(Cr)@xerogel, in which no water was added (Fig. A.14). The 35 wt% MIL-101(Cr)@xerogel-H₂O has the MIL crystallites slightly more separated from the xerogel, while the 35 wt% MIL-101(Cr)@xerogel (no H₂O) shows the MIL and xerogel more intimately mixed.

Subsequently addition of water also significantly increased the surface areas and total pore volumes in case of the 35, 46 and 50 wt% MIL-101(Cr)@xerogel-composites (Table 1).

Table 1.

Pore size distribution curves of the bulk MILs, can be calculated from the nitrogen adsorption isotherms (Fig. 7) using NLDFT models and show pores sizes of 12, 15, 18–19 and 20–21 Å for *MIL-100(Fe)* and *MIL-100(Cr)*. The pore regions of 18–19 and 20–21 Å correspond to the MIL-100 cages (Fig. A.17).

The pore size distribution curve of bulk MIL-101(Cr) shows pores of 12 and 15 Å in diameter, which are consistent with the pentagonal (12 Å) and hexagonal windows (14.7–16 Å) (Fig. A.16) [42]. The larger pores of 19 and 24 Å belong to the cages with diameters of 29 and 34 Å (Fig. A.16) [42]. Differences to the cage size from X-ray structure refinement was seen before can be explained by residual impurities of non-coordinated ligand and metal-ligand fragments inside the pores [74].

Pore size distribution curves of the MIL@xerogel composites match those of the respective bulk MIL. Thus, from N₂ sorption isotherms, BET surface area and pore diameter distribution it is obvious that all monolithic composite materials largely retain the accessibility to the micro- and mesopores of the MIL. This is, however, only true for the materials based on pre-polymerized xerogel solutions. In contrast, a MIL-100(Cr)@xerogel composite without any

pre-polymerization of the xerogel solution, presents a material which appears non-porous or without any accessible porosity (Table 1, see 'I'; Fig. A.8, A.9, A.10).

Other MOF composite materials show similar differences between experimental and estimated BET surface areas (Table 2). HKUST-1, embedded in porous carbon monoliths achieves only 40% of the estimated BET surface areas [45]. Composites like UiO-66@polyurethane or HKUST@HIPE reach about 60% of the calculated values [53,75,76]. These values are comparable to our pre-polymerized MIL-100(M)@xerogel (M = Fe, Cr) compounds. Yet, metal-organic frameworks in inorganic silica templates, such as HKUST-1 incorporated in silica aerogels or HKUST-1 in macro-/mesoporous silica match or even exceed the estimated BET values similar to the MIL-101(Cr)@xerogel composites with added water reported here [52,58].

Table 2.

In order to evaluate the monolithic composites as potential adsorbents for heat transformation applications, water sorption experiments were carried out to quantify their hydrophilic behavior. Water sorption isotherms of different MIL@xerogel materials are shown together with the adsorption isotherm of bulk MIL and R,F-xerogel (Fig. 8a-c). MIL-100@xerogel composites display the same stepwise adsorption isotherm, as for bulk MIL-100(M) (M = Fe, Cr) (Fig. 8a-b, Fig. A.2b, Fig. A.4b). This specific shape relates to the stepwise filling of the different MIL-100 cages. Mesopores larger than 20 Å (2 nm) for MIL-100(Cr)@xerogel samples probably influence the water adsorption characteristics of these composites (Table 1, Fig. 7).

Figure 8.

Water loading capacities at $P \cdot P_0^{-1} = 0.9$ of the MIL@xerogel compounds can be estimated (calculated) from the MIL wt% based on the water uptake of bulk MIL using formula (II) in Table 1. MIL-100(M)@xerogel (M = Fe, Cr) compounds reach approximately 74 % of the calculated values. The MIL-101(Cr)@xerogel monoliths with 35 and 46 wt% of MIL loading achieve 93 % of the estimated water uptake capacities. Compared to the BET analyses given above, the MIL-101(Cr) water uptakes are closer to the calculated expected values. The 77 wt% loaded MIL-101(Cr)@xerogel-H₂O matches or even slightly exceeds the estimated water uptake capacity as a result of the higher BET surface area (Table 1). As an indication of the hierarchical nature the 35 and 46 wt% MIL-101(Cr) composites achieve a near to maximum water loading already at $P \cdot P_0^{-1} = 0.5$ (Fig. 5c). The 77 wt% MIL-101(Cr)@xerogel-H₂O composites already realizes 0.79 g·g⁻¹ water uptake at $P \cdot P_0^{-1} = 0.5$ (Fig. 5c). Whereas for bulk MIL-101(Cr) only 0.57 g·g⁻¹, corresponding to ~50% water uptake could be achieved at $P \cdot P_0^{-1} = 0.5$.

When calculating the water adsorption value relative to the surface area measured in the MIL@xerogel composite (last column in Table 1) the following trends became apparent: For the iron and chromium MIL-100@xerogel composites the surface-based water adsorption is higher than for the MIL-100 alone. This suggests that our method of encapsulation of MOFs leads to a high dispersion of the MILs in the xerogel matrix. For the MIL-101(Cr) composite (prepared with added water) and bulk MIL-101(Cr) the surface area-based water uptake values of $0.35 \times 10^{-3} \text{ g} \cdot \text{m}^{-2}$ are mostly the same. This is in agreement with the good match between the measured and calculated (mass-weighted) BET values for the composites prepared with added water. There is no pore blocking for the MIL-101(Cr)@xerogel-H₂O materials. The MIL-100(Cr) composite has a significantly higher surface area-based water adsorption value than the MIL-100(Fe) composite. This is explained by the hierarchical contribution of the xerogel matrix which adds significantly with diameters > 20 Å for the chromium and less for the iron material according to the pore diameter distribution plots in Fig. 8 d and b (see Supporting Information).

4. Conclusion

We presented new composite materials in monolithic shape based on a metal-organic framework part (MIL-100(M)/101(Cr), (M = Fe, Cr)) and a polymerized resorcinol-formaldehyde xerogel as the binding agent. Mesoporous resorcinol-formaldehyde (R,F-) xerogels are easily obtainable, highly tunable and the second most investigated xerogels (after silica xerogels). The MIL@xerogel composites were characterized by powder X-ray diffraction, infrared spectroscopy, nitrogen- and water sorption and scanning electron microscopy. Embedding up to 77 wt% of MIL particles is possible without the loss of the mechanical stability of the monoliths. Pore blocking effects of the MILs through the binding agent could largely be avoided by pre-polymerization of the native xerogel solution before embedding of the MILs. The larger MIL-101(Cr) pores remain more open than the smaller MIL-100 pores during the monolith syntheses. The expected BET surface areas and water uptakes could be reached when the MIL was added together with water to the pre-polymerized xerogel solution. Formation of a water film around the MIL particles may be responsible to avoid pore blocking. The MIL-101(Cr)@xerogel-H₂O composites then match the wt%-correlated BET values and water uptakes within experimental error. As an indication of the hierarchical nature the 77 wt% MIL-101(Cr)@xerogel-H₂O composite achieves 0.79 g·g⁻¹ water uptake at $P/P_0 = 0.5$ while for bulk MIL-101(Cr) only 0.57 g·g⁻¹ water uptake could be achieved at $P/P_0 = 0.5$. Also, the surface area-based water adsorption is higher for the MIL-100@xerogel composites than for MIL-100 alone.

Appendix A. Supplementary A

Supplementary data associated with this article can be found, in the online version, at doi:

Acknowledgements

Support by the DAAD with PPP-project no 57053987 ("hierarchical structured metal-based nanocomposites") and the University of Düsseldorf through its strategic research fund (SFF) is gratefully acknowledged. We thank Mr. Steffen Köhler for help with the SEM images. Marina Schwan and Jessica Laskowski from DLR, Cologne for the kind introduction to xerogel syntheses. We thank one of the referees for emphasizing the water adsorption value relative to the surface area.

References

-
- [1] (a) S.R. Batten, N.R. Champness, X.-M. Chen, J. Garcia-Martinez, S. Kitagawa, L. Öhrström, M. O'Keeffe, M.P. Suh, J. Reedijk, *CrystEngComm* 14 (2012) 3001–3004. (b) S.R. Batten, N.R. Champness, X.-M. Chen, J. Garcia-Martinez, S. Kitagawa, L. Öhrström, M. O'Keeffe, M.P. Suh, J. Reedijk, *Pure Appl. Chem.* 85 (2013) 1715–1724.
- [2] J.R. Long, O.M. Yaghi, *Chem. Soc. Rev.* 38 (2009) 1213–1214.
- [3] C. Serre, S. Kitagawa, P.D.C. Dietzel, *Microporous Mesoporous Mater.* 157 (2012) 1–2.
- [4] M. Yoon, R. Srirambalaji, K. Kim, *Chem. Rev.* 112 (2012) 1196–1231.
- [5] A. Herbst, A. Khutia, C. Janiak, *Inorg. Chem.* 53 (2014) 7319–7333.
- [6] F.X. Llabrés i Xamena, F.G. Cirujano, A. Corma, *Microporous Mesoporous Mater.* 157 (2012) 112–117.
- [7] R.B. Getman, Y.-S. Bae, C.E. Wilmer, R.Q. Snurr, *Chem. Rev.* 112 (2012) 703–723.
- [8] Z. Chen, S. Xiang, H.D. Arman, P. Li, S. Tidrow, D. Zhao, B. Chen, *Eur. J. Inorg. Chem.* 24 (2010) 3745–3749.
- [9] L. Wu, M. Xue, S.-L. Qiu, G. Chaplais, A. Simon-Masseron, J. Patarin, *Microporous Mesoporous Mater.* 157 (2012) 75–81.
- [10] Z. Zhang, Y. Zhao, Q. Gong, Z. Li, J. Li, *Chem. Commun.* 49 (2013) 653–661.
- [11] J.-R. Li, Y. Ma, M.C. McCarthy, J. Sculley, J. Yu, H.-K. Jeong, P.B. Balbuena, H.-C. Zhou, *Coord. Chem. Rev.* 155 (2011) 1791–1823.
- [12] Z.R. Herm, R. Krishna, J.R. Long, *Microporous Mesoporous Mater.* 157 (2012) 94–100.
- [13] M.G. Plaza, A.F.P. Ferreira, J.C. Santos, A.M. Ribeiro, U. Müller, N. Trukhan, J.M. Loureiro, A.E. Rodrigues, *Microporous Mesoporous Mater.* 157 (2012) 101–111.
- [14] C. Janiak, *Dalton Trans.* 14 (2003) 2781–2804.
- [15] C. Janiak, J.K. Vieth, *New J. Chem.* 34 (2010) 2366–2388.
- [16] G. Férey, *Chem. Soc. Rev.* 37 (2008) 191–214.
- [17] N. Stock, S. Biswas, *Chem. Rev.* 112 (2012) 933–969.

-
- [18] M. Gaab, N. Trukhan, S. Maurer, R. Gummaraju, U. Müller, *Microporous Mesoporous Mater.* 157 (2012) 131–136.
- [19] C. Li, J. Zhou, Y. Cao, J. Zhong, Y. Liu, C. Kang, Y. Tan, *Appl. Energ.* 117 (2014) 149–156.
- [20] (a) Y.I. Aristov, *Int. J. Refrigeration* 32 (2009) 675–686. (b) B.B. Saha, A. Chakraborty, S. Koyama, Y.I. Aristov, *Int. J. Heat Mass Transfer* 52 (2009) 516–524. (c) R.E. Critoph, Z. Tamainot-Telto, S.J. Metcalf, *Int. J. Refrigeration* 32 (2009) 1212–1229. (d) J.V. Veselovskaya, R.E. Critoph, R.N. Thorpe, S. Metcalf, M.M. Tokarev, Y.I. Aristov, *Appl. Therm. Eng.* 30 (2010) 1188–1192.
- [21] K. Habib, B.B. Saha, A. Chakraborty, S.T. Oh, S. Koyama, *Appl. Therm. Eng.* 50 (2013) 1582–1589.
- [22] A.A. Askalany, M. Salem, I.M. Ismael, A.H.H. Ali, M.G. Morsy, B.B. Saha, *Renew. Sust. Energ. Rev.* 19 (2013) 565–572.
- [23] D. Fröhlich, S.K. Henninger, C. Janiak, *Dalton Trans.* 43 (2014) 15300–15304.
- [24] S.K. Henninger, H.A. Habib, C. Janiak, *J. Am. Chem. Soc.* 131 (2009) 2776–2777.
- [25] S.K. Henninger, F. Jeremias, H. Kummer, C. Janiak, *Eur. J. Inorg. Chem.* (2012) 2625–2634.
- [26] F. Jeremias, L. Lozan, S.K. Henninger, C. Janiak, *Dalton Trans.* 42 (2013) 15967–15973.
- [27] J. Canivet, A. Fateeva, Y. Guo, B. Coasne, D. Farrusseng, *Chem. Soc. Rev.* 43 (2014) 5594–5617.
- [28] J. Canivet, J. Bonnefoy, C. Daniel, A. Legrand, B. Coasne, D. Farrusseng, *New J. Chem.* 38 (2014) 3102–3111.
- [29] J. Ehrenmann, S.K. Henninger, C. Janiak, *Eur. J. Inorg. Chem.* (2011) 471–474.
- [30] M. Wickenheisser, F. Jeremias, S.K. Henninger, C. Janiak, *Inorg. Chim. Acta* 407 (2013) 145–152.
- [31] G. Akiyama, R. Matsuda, H. Sato, A. Hori, M. Takata, S. Kitagawa, *Microporous Mesoporous Mater.* 157 (2012) 89–93.
- [32] A. Khutia, H.U. Rammelberg, T.S. Schmidt, S. Henninger, C. Janiak, *Chem. Mater.* 25 (2013) 790–798.
- [33] J.B. De Coste, G.W. Peterson, B.J. Schindler, K.L. Killops, M.A. Browe, J.J. Mahle, *J. Mater. Chem. A* 1 (2013) 11922–11932.
- [34] F. Jeremias, D. Fröhlich, C. Janiak, S.K. Henninger, *New J. Chem.* 38 (2014) 1846–1852.
- [35] F. Jeremias, A. Khutia, S.K. Henninger, C. Janiak, *J. Mater. Chem.* 22 (2012) 10148–10151.

-
- [36] G. Férey, C. Serre, C. Mellot-Draznieks, F. Millange, S. Surble, J. Dutour, I. Margiolaki, *Angew. Chem. Int. Ed.* 43 (2004) 6296–6301.
- [37] G. Akiyama, R. Matsuda, S. Kitagawa, *Chem. Lett.* 39 (2010) 360–361.
- [38] P. Horcajada, S. Surble, C. Serre, D.-Y. Hong, Y.-K. Seo, J.-S. Chang, J.-M. Grenèche, I. Margiolaki, G. Férey, *Chem. Commun.* 27 (2007) 2820–2822.
- [39] J.S. Lee, S.H. Jung, J.W. Yoon, Y.K. Hwang, J.-S. Chang, *J. Ind. Eng. Chem.* 15 (2009) 674–676.
- [40] L. Kurfiřtová, Y.-K. Seo, Y.-K. Hwang, J.-S. Chang, J. Čejka, *Catal. Today* 179 (2012) 85–90.
- [41] P. Küsgens, M. Rose, I. Senkovska, H. Fröde, A. Henschel, S. Siegle, S. Kaskel, *Microporous Mesoporous Mater.* 120 (2009) 325–330.
- [42] G. Férey, C. Mellot-Draznieks, C. Serre, F. Millange, J. Dutour, S. Surble, I. Margiolaki, *Science* 309 (2005) 2040–2042.
- [43] B. Böhlinger, R. Fischer, M.R. Lohe, M. Rose, S. Kaskel, P. Küsgens, *Metal-Organic Frameworks: Applications from Catalysis to Gas Storage*, Edited by D. Farrusseng, 1st ed., Wiley-VCH Verlag GmbH & Co. KGaA, Weinheim, 2011, chapter 15, pp. 353–381.
- [44] (a) F. Jeremias, S.K. Henninger, C. Janiak, *Chem. Commun.* 48 (2012) 9708–9710. (b) F. Jeremias, D. Fröhlich, C. Janiak, S.K. Henninger, *RSC Advances* 4 (2014) 24073–24082.
- [45] D. Qian, C. Lei, G. Hao, W. Li, A. Lu, *ACS Appl. Mater. Interfaces* 4 (2012) 6125–6132.
- [46] M. Wickenheisser, C. Janiak, *Microporous Mesoporous Mater.* 204 (2015) 242–250.
- [47] V. Finsy, L. Ma, L. Alaerts, D.E. De Vos, G.V. Baron, J.F.M. Denayer, *Microporous Mesoporous Mater.* 120 (2009) 221–227.
- [48] R. Zacharia, D. Cossement, L. Lafi, R.J. Chahine, *Mater. Chem.* 20 (2010) 2145–2151.
- [49] M.R. Lohe, M. Rose, S. Kaskel, *Chem. Commun.* (2009) 6056–6058.
- [50] H.B. Tanh Jeazet, C. Staudt, C. Janiak, *Chem. Commun.* 48 (2012) 2140–2142.
- [51] P. Küsgens, A. Zgaverdea, H. Fritz, S. Siegle, S. Kaskel, *J. Am. Ceram. Soc.* 93 (2010) 2476–2479.
- [52] A. Sachse, R. Ameloot, B. Coq, F. Fajula, B. Coasne, D. De Vos, A. Galarneau, *Chem. Commun.* 48 (2012) 4749–4751.
- [53] M.G. Schwab, I. Senkovska, M. Rose, M. Koch, J. Pahnke, G. Jonschker, S. Kaskel, *Adv. Eng. Mat.* 10 (2008) 1151–1155.
- [54] H. Huang, C. Lin, C. Wu, Y. Cheng, C. Lin, *Anal. Chim. Acta* 779 (2013) 96–103.
- [55] (a) H.B. Tanh Jeazet, C. Staudt, C. Janiak, *Dalton Trans.* 41 (2012) 14003–14027. (b) H.B. Tanh Jeazet, C. Janiak, *Metal-Organic Framework Materials*, Edited by L.R. MacGillivray and C.M. Lukehart, John Wiley & Sons, Ltd, Chichester, 2014, pp 1–15.
- [56] N. Hüsing, U. Schubert, *Angew. Chem.* 110 (1999) 22–47.

-
- [57] (a) J. Li, J. Li, H. Meng, S. Xie, B. Zhang, L. Li, H. Ma, J. Zhang, M. Yu, *J. Mater. Chem. A* 2 (2014) 2934–2941. (b) M.A. Aegerter, N. Leventis, Edited by M.M. Koebel, *Aerogels Handbook*, Springer, New York, 2011.
- [58] Z. Ulker, I. Erucar, S. Keskin, C. Erkey, *Microporous Mesoporous Mater.* 170 (2013) 352–358.
- [59] U. Fischer, R. Saliger, V. Bock, R. Petricevic, J.J. Fricke, *Porous Mater.* 4 (1997) 281–285.
- [60] S.A. Al-Muhtaseb, J.A. Ritter, *Adv. Mater.* 15 (2003) 101–114.
- [61] J. Laskowski, B. Milow, L. Ratke, *Microporous Mesoporous Mater.* 197 (2014) 308–315.
- [62] (a) N. Rey-Raap, J. Angel Menéndez, A. Arenillas, *Microporous Mesoporous Mater.* 195 (2014) 266–275. (b) C. Lin, J.A. Ritter, *Carbon* 35 (1997) 1271–1278. (c) S. Mulik, C. Sotiriou-Leventis, N. Leventis, *Chem. Mater.* 19 (2007) 6138–6144. (d) M. Reuß, L.J. Ratke, *Sol-Gel Sci. Technol.* 47 (2008) 74–80. (e) M. Schwan, L. Ratke, *J. Mater. Chem. A* 1 (2013) 13462–13468.
- [63] B. Nagy, O. Czakkel, K. László, *Microporous Mesoporous Mater.* 185 (2014) 66–71.
- [64] L.D. Gelb, K.E. Gubbins, R. Radhakrishnan, M. Sliwinski-Bartowiak, *Rep. Prog. Phys.* 62 (1999) 1573–1659.
- [65] N.A. Sedron, J.P.R.B. Walton, N. Quirke, *Carbon* 27 (1989) 853–861.
- [66] A. Vishnyakov, P. Ravikovitch, A.V. Neimark, *Langmuir* 16 (2000) 2311–2320.
- [67] J.W. Yoon, Y.-K. Seo, Y.K. Hwang, J.-S. Chang, H. Leclerc, S. Wuttke, P. Bazin, A. Vimont, M. Daturi, E. Bloch, P.L. Llewellyn, C. Serre, P. Horcajada, J.-M. Grenèche, A.E. Rodrigues, G. Férey, *Angew. Chem. Int. Ed.* 49 (2010) 5949–5952.
- [68] A. Vimont, J.-M. Goupil, J.-C. Lavalley, M. Daturi, S. Surblé, C. Serre, F. Millange, G. Férey, N. Audebrand, *J. Am. Chem. Soc.* 128 (2006) 3218–3227.
- [69] J. Yang, Q. Zhao, J. Li, J. Dong, *Microporous Mesoporous Mater.* 130 (2010) 174–179.
- [70] A. Awadallah-F, A.M. Elkhatat, S.A. Al-Muhtaseb, *J. Mater. Sci.* 46 (2011) 7760–7769.
- [71] K.S.W. Sing, D.H. Everett, R.A.W. Haul, L. Moscou, R.A. Pierotti, J. Rouquerol, T. Siemieniowska, *Pure Appl. Chem.* 57 (1985) 603–619.
- [72] R. Saliger, V. Bock, R. Petricevic, T. Tillotson, S. Geis, J. Fricke, *J. Non-Cryst. Solids* 221 (1997) 144–150.
- [73] W. Chen, Z. Zhang, W. Bao, Y. Lai, J. Li, Y. Gan, J. Wang, *Electrochim. Acta* 134 (2014) 293–301.
- [74] R. Canioni, C. Roch-Marchal, F. Sécheresse, P. Horcajada, C. Serre, M. Hardi-Dan, G. Férey, J.-M. Grenèche, F. Lefebvre, J.-S. Chang, Y.-K. Hwang, O. Lebedev, S. Turner, G.J. Van Tendeloo, *Mater. Chem.* 21 (2011) 1226–1233.
- [75] M. L. Pinto, S. Dias, J. Pires, *Appl. Mater. Interfaces* 5 (2013) 2360–1263.
- [76] L.D. O'Neill, H. Zhang, D.J. Bradshaw, *J. Mater. Chem.* 20 (2010) 5720–5726.

Tables / Figure captions

Table 1. Nitrogen and water vapor sorption measurements.

Sample ^a	Textural data			Water adsorption value ^e		
	S(BET) meas. ^b (m ² ·g ⁻¹)	S(BET) calc. ^c (m ² ·g ⁻¹)	V(pore), (cm ³ ·g ⁻¹) ^d	meas. ^e (g·g ⁻¹)	calc. ^f (g·g ⁻¹)	rel. to surf- ace area ^g (x 10 ⁻³ g m ⁻²)
R,F-xerogel	100	--	0.16	0.10	--	
MIL-100(Fe)	2200 ^h	--	0.94	0.76 ⁱ	--	0.35
Composites:						
43 wt%	590	1000	0.31	0.26	0.38	0.44
50 wt%	730	1150	0.39	0.33	0.43	0.45
58 wt%	770	1320	0.41	n.d. ^j		
MIL-100(Cr)	1560 ^k		0.85	0.60 ⁱ		0.38
Composites: ^m						
41 wt%	400	700	0.28	0.23	0.31	0.57
51 wt%	550	850	0.35	0.28	0.36	0.51
56 wt%	570	920	0.40	n.d. ^j		
MIL-101(Cr)	3060 ⁿ		1.45	1.06 ^o		0.35
Composites: ^p	standard/with water added		standard/with water added	standard/with water added		
35 wt%	960 / 1340	1140	0.54 / 0.69	n.d / 0.41	0.44	0.31
46 wt%	1160 / 1420	1460	0.62 / 0.72	n.d. / 0.50	0.54	0.35
50 wt%	1350 / 1500	1580	0.72 / 0.76	n.d.		
77 wt%	- / 2530	2380	- / 1.27	- / 0.88	0.84	0.35

^a wt% refers to MIL amount in the composites.

^b S(BET) measured from N₂ sorption isotherm 77 K with a standard deviation ± 20 m²·g⁻¹ (calculated at 0.05 < P·P₀⁻¹ < 0.2).

^c S(BET) calculated (estimated) as the sum of the mass-weighted surface areas of the MILs (MIL-100(Fe) = 2200 m²·g⁻¹; MIL-100(Cr) = 1560 m²·g⁻¹; MIL-101(Cr) = 3060 m²·g⁻¹) and R,F-xerogel (100 m²·g⁻¹) from the following formula (l):

$$\text{BET calc} = \frac{\text{wt\% of xerogel}}{100} \times 100 \text{ m}^2 \cdot \text{g}^{-1} + \frac{\text{wt\% of MIL}}{100} \times 2200 \text{ (MIL - 100Fe) or } 1560 \text{ (MIL - 100Cr) or } 3060 \text{ (MIL - 101Cr) m}^2 \cdot \text{g}^{-1}$$

^d Total pore volume V(pore) calculated from N₂ sorption isotherm at 77 K (P·P₀⁻¹ = 0.95) for pores ≤ 20 nm.

^e Water adsorption value measured from water sorption isotherm at 293 K (P·P₀⁻¹ = 0.9).

^f **Water adsorption value calculated** (estimated) as the sum of the mass-weighted uptakes at $P/P_0^{-1} = 0.9$ of the MILs (MIL-100(Fe) = $0.76 \text{ g}\cdot\text{g}^{-1}$; MIL-100(Cr) = $0.60 \text{ g}\cdot\text{g}^{-1}$; MIL-101(Cr) = $1.06 \text{ g}\cdot\text{g}^{-1}$) and R,F-xerogel ($0.10 \text{ g}\cdot\text{g}^{-1}$) from the following formula (II):

Water adsorption calc =

$$\frac{\text{wt\% of xerogel}}{100} \times 0.10 \text{ g}\cdot\text{g}^{-1} + \frac{\text{wt\% of MIL}}{100} \times 0.76 \text{ (MIL - 100Fe) or } 0.60 \text{ (MIL - 100Cr) or } 1.06 \text{ (MIL - 101Cr) g}\cdot\text{g}^{-1}$$

^g **Water adsorption value calculated** relative to the measured BET surface area of the MIL or MIL@xerogel composite according to the following formula (III):

$$\text{Water adsorption calculated relative to surface area} = \frac{\text{water adsorption measured in g}\cdot\text{g}^{-1}}{\text{S(BET) measured in m}^2\cdot\text{g}^{-1}} \text{ [g}\cdot\text{m}^{-2}]$$

for example: for MIL-100(Fe): $0.76 \text{ g}\cdot\text{g}^{-1} / 2200 \text{ m}^2\cdot\text{g}^{-1} = 0.00035 \text{ g}\cdot\text{m}^{-2} = 0.35 \times 10^{-3} \text{ g}\cdot\text{m}^{-2}$;
43 wt% MIL-100(Fe)@xerogel composite: $0.26 \text{ g}\cdot\text{g}^{-1} / 590 \text{ m}^2\cdot\text{g}^{-1} = 0.00044 \text{ g}\cdot\text{m}^{-2} = 0.44 \times 10^{-3} \text{ g}\cdot\text{m}^{-2}$;

^h in literature $1550\text{--}2050 \text{ m}^2\cdot\text{g}^{-1}$ [38,39].

ⁱ in literature $0.65\text{--}0.75 \text{ g}\cdot\text{g}^{-1}$ [35,40].

^j n.d. = not determined.

^k in literature $1770\text{--}1980 \text{ m}^2\cdot\text{g}^{-1}$ [38,39].

^l in literature $0.6\text{--}0.7 \text{ g}\cdot\text{g}^{-1}$ [37].

^m MIL-100(Cr)@xerogel without any pre-polymerization of the xerogel solution yielded a BET surface area of $20 \text{ m}^2\cdot\text{g}^{-1}$ and a total pore volume of $0.03 \text{ cm}^3\cdot\text{g}^{-1}$ (see supplementary data for details).

ⁿ in literature $2060\text{--}4100 \text{ m}^2\cdot\text{g}^{-1}$ [29,42].

^o in literature $1.0\text{--}1.5 \text{ g}\cdot\text{g}^{-1}$ [29,41].

^p The first value refers to the standard syntheses of MIL-101(Cr)@xerogel, the second value to the synthesis of MIL-101(Cr)@xerogel-H₂O composites where additional water was used.

Table 2. Comparison of N₂ sorption data of similar composite materials from the literature.

Composites	Experimental S(BET) (m ² ·g ⁻¹)	Estimated S(BET) (m ² ·g ⁻¹) ^f	wt% of MOFs and quantification method	Possible application	Ref.
HKUST-1 @PAM ^a	654 ^d	667	62 wt%; N ₂ sorption data + TGA	no application investigated	[76]
HKUST-1 monolith ^b	484 ^e	-	No wt% given	no application investigated	[51]
HKUST-1 @porous carbon monoliths	270; 455; 516	816; 988; 1198	19 wt%; 41 wt%; 68 wt%; Weighing method	CO ₂ storage; Gas separation (CO ₂ / N ₂)	[45]
HKUST-1 @silica aerogel	1025; 1036; 1138	944; 955; 1056	4.2 wt%; 16.3 wt%; 30.5 wt%; Weighing method	no application investigated	[58]
HKUST-1 @macro- /mesoporous silica	971	907	25 wt%; TGA	catalysis	[52]
UiO-66@ polyurethane	511 ^d ; 427 ^d	834; 752	71 wt%; 64 wt%; TGA	adsorption of organic vapors	[75]
HKUST-1 @HIPE	570	846	62.3 wt%; TGA	no application investigated	[53]

CAU-1@PMMA	423	-	No wt% given	open-tubular capillary electrochromatography	[69]
------------	-----	---	--------------	--	------

^a PAM = polyacrylamide. We notice that MOF wt% determination in HKUST-1@PAM composites was calculated from nitrogen sorption data based on the assumption that all of the native MOF surface area is still accessible in the composite material.

^b binding agent: methoxy functionalized siloxane ether; plasticizer: methyl hydroxyl propyl cellulose.

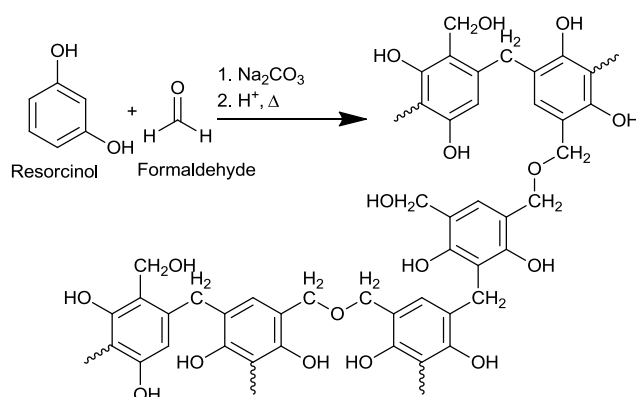
^c PMMA = polymethyl methacrylate.

^d BET surface areas of pure binding agents are not considered in calculations due to their absence in the corresponding literature.

^e Values decreased after several months to 287 m²·g⁻¹.

^f BET surface area as the sum of the mass-weighted surface areas of MOFs and porous binding agents calculated from the following formula:

$$\text{BET (estimated)} = \frac{\text{wt\% of MOF}}{100} \times \text{BET of pure MOF} + \frac{\text{wt\% of binding agent}}{100} \times \text{BET of pure binding agent}$$



Scheme 1. Schematic presentation of the polymerization reaction of resorcinol (R) with formaldehyde (F) in the presence of a base (C).

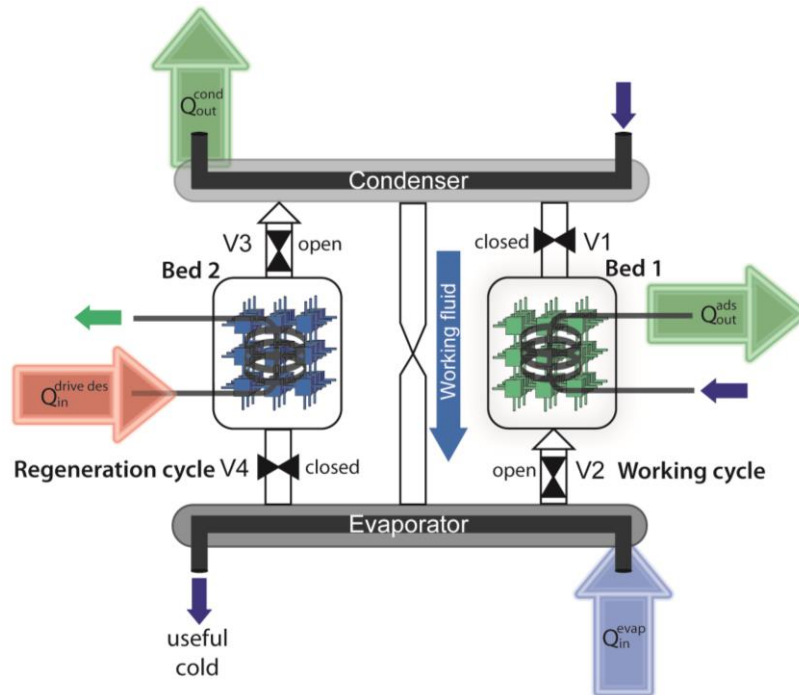


Fig. 1. Thermodynamic principle for adsorption chillers or heat pumps. Bed 1 (here in working cycle) and bed 2 (here in regeneration cycle) contain the porous adsorbent [24]. $Q_{in}^{drive,des}$ driving heat of desorption at a high temperature level (red), Q_{out}^{cond} and Q_{out}^{ads} , heat of condensation and heat of adsorption at a medium temperature level (green), Q_{in}^{evap} heat of evaporation at a low temperature level (blue).

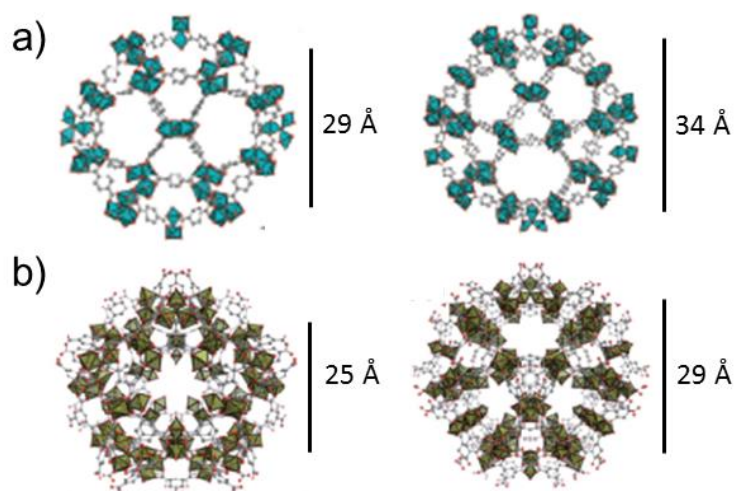


Fig. 2. a) MIL-101(Cr) small and large cages (CSD-Refcode OCUNAK [42]). b) Small cage and large cage in MIL-100(Fe) (CSD-Refcode CIGXIA [38]) (different objects are not drawn to scale). Hydrogen atoms and solvent molecules of crystallization are not shown. MIL-100(Cr) is isostructural to MIL-100(Fe). See Fig. A.16 and Fig. A17 for further details.

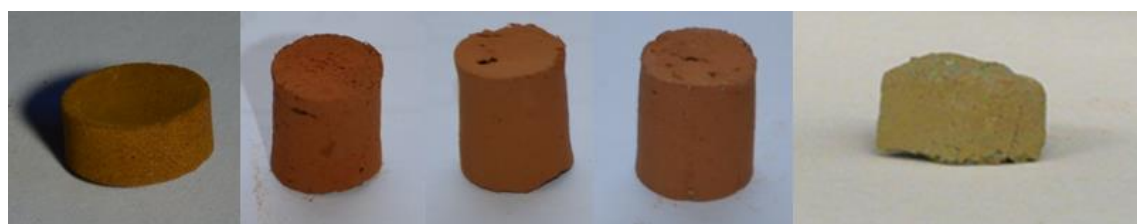


Fig. 3. From left to right: Pure R,F-xerogel, MIL@xerogel composites with 58 wt% MIL-100(Fe), 41 wt% MIL-100(Cr), 50 wt% MIL-101(Cr) and 77 wt% MIL-101(Cr) (77 wt%, MIL-101(Cr)@xerogel-H₂O). Dimensions (diameter x height) are 13 x 8 mm for pure R-F-xerogel; 10 x 13 mm for both MIL-100@xerogel; 10 x 14 mm for MIL-101(Cr)@xerogel (50 wt%) and 15 x 10 mm for MIL-101(Cr)@xerogel-H₂O (77 wt%). MIL-101(Cr)@xerogel-H₂O was cut to show the MIL distribution inside the monolith.

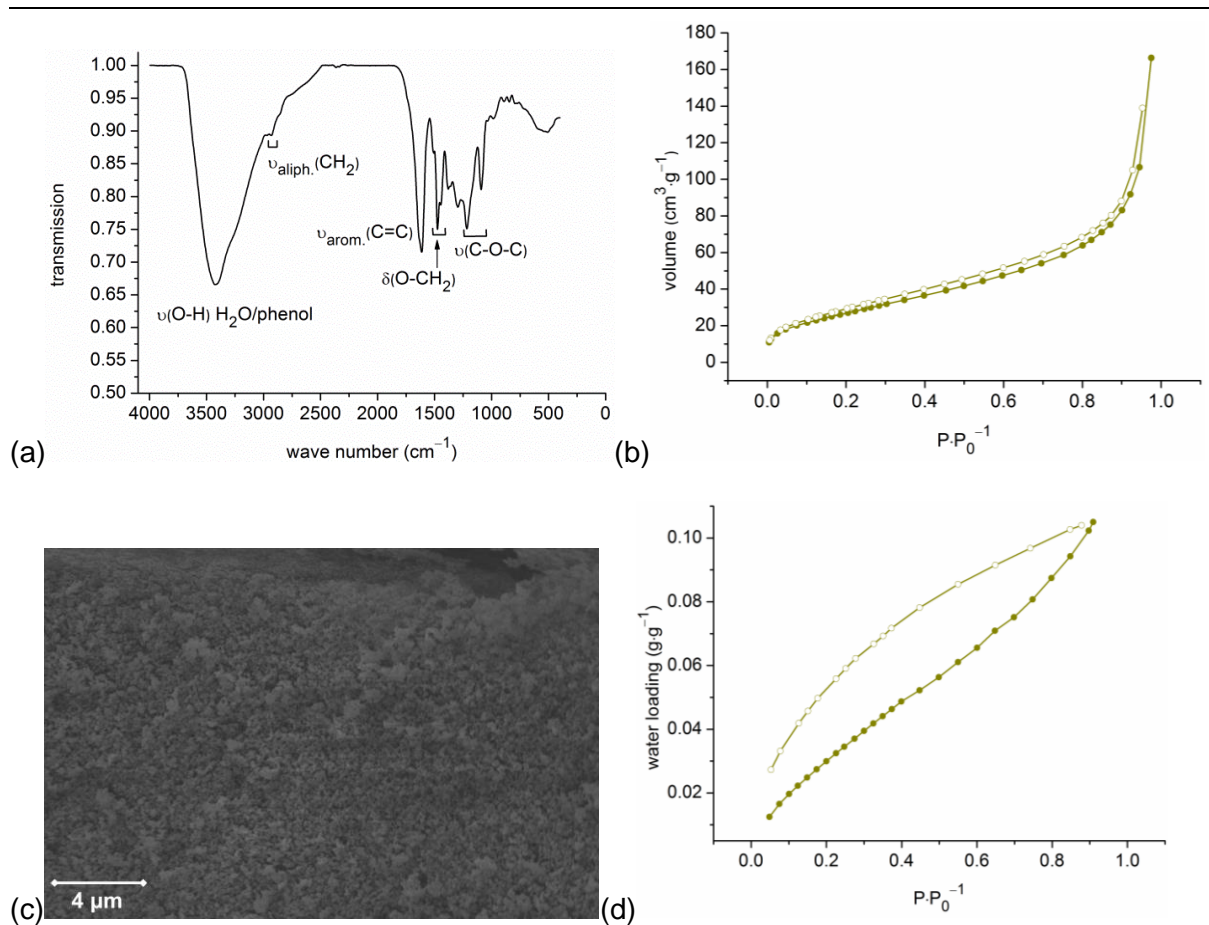
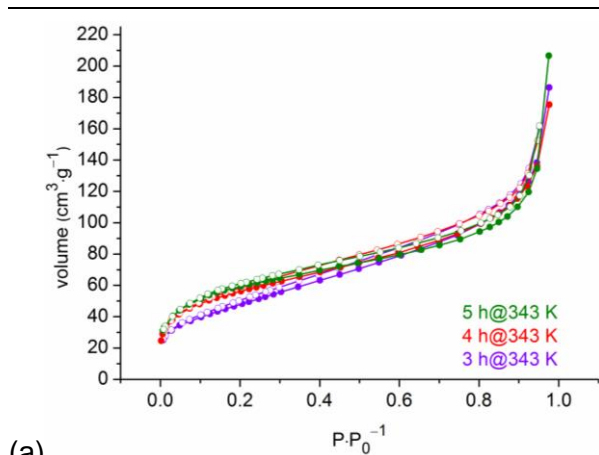
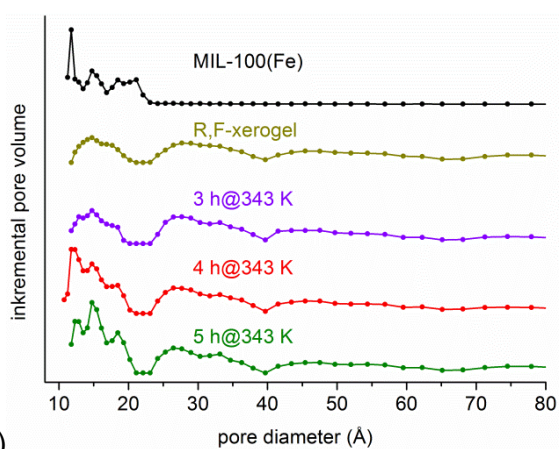


Fig. 4. Native or bulk R,F-xerogel (a) IR-spectrum (KBr), (b) N₂-sorption isotherm (degassing conditions: 3 h, 423 K), (c) scanning electron microscopy (SEM) image, (d) water vapor sorption isotherm (degassing conditions: 3 h, 423 K). Adsorption is depicted with filled, desorption with empty symbols.



(a)



(b)

Fig. 5. (a) N_2 -sorption isotherms of MIL-100(Fe)@xerogel with 11 wt% MIL-100(Fe). MIL-100(Fe) powders were added to the R,F-xerogel solutions after 3, 4 and 5 h of pre-polymerization time at 343 K, respectively (degassing conditions: 3 h, 423 K, $S(BET) = 180 \text{ m}^2 \cdot \text{g}^{-1}$ (3 h), $210 \text{ m}^2 \cdot \text{g}^{-1}$ (4 h), $220 \text{ m}^2 \cdot \text{g}^{-1}$ (5 h)). (b) Pore size distribution curves of native MIL-100(Fe), native R,F-xerogel and MIL-100(Fe)@xerogel with 11 wt% MIL-100(Fe) (3, 4 and 5 h of polymerization at 343 K). Adsorption is depicted with filled, desorption with empty symbols.

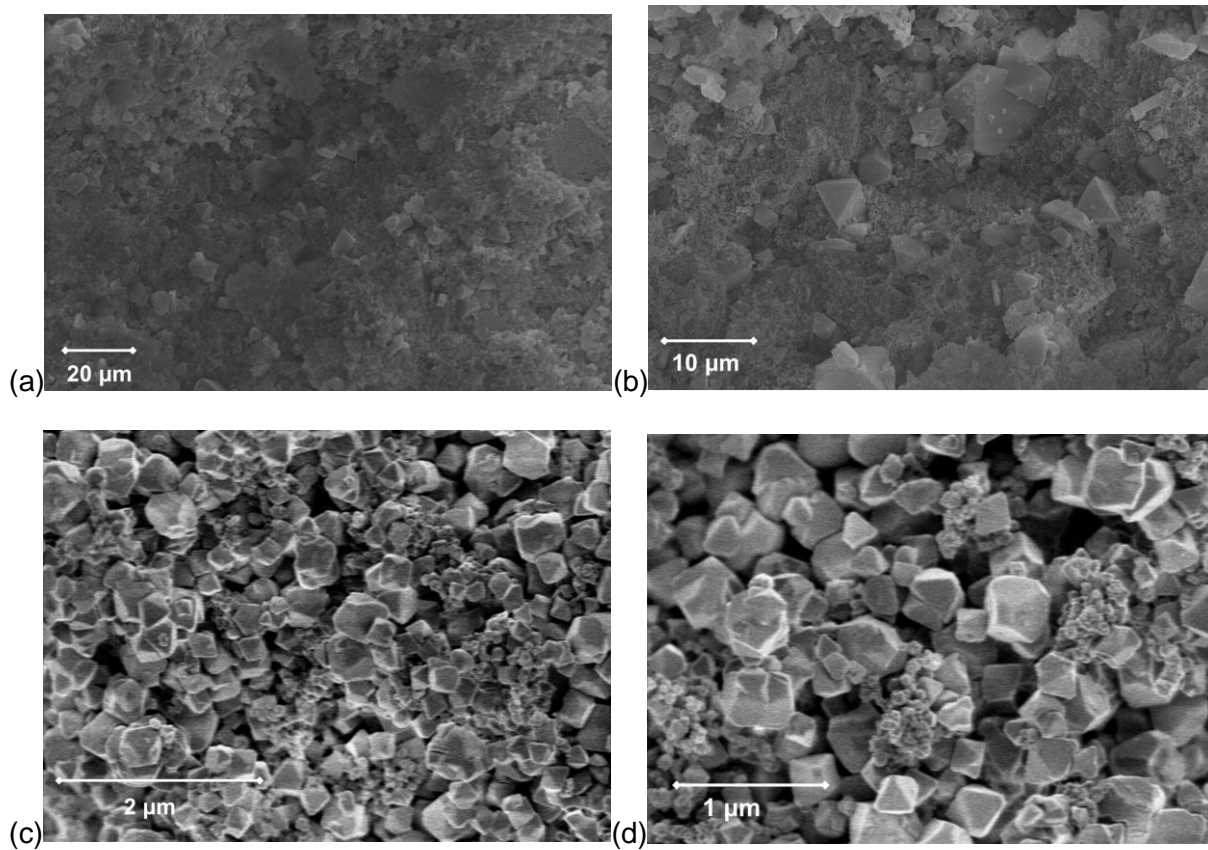


Fig. 6. Scanning electron microscopy (SEM) images of (a)-(b) MIL-100(Fe)@xerogel (43 wt% MIL-100(Fe)) and (c)-(d) MIL-101(Cr)@xerogel-H₂O (77 wt% MIL-101(Cr)) composites.

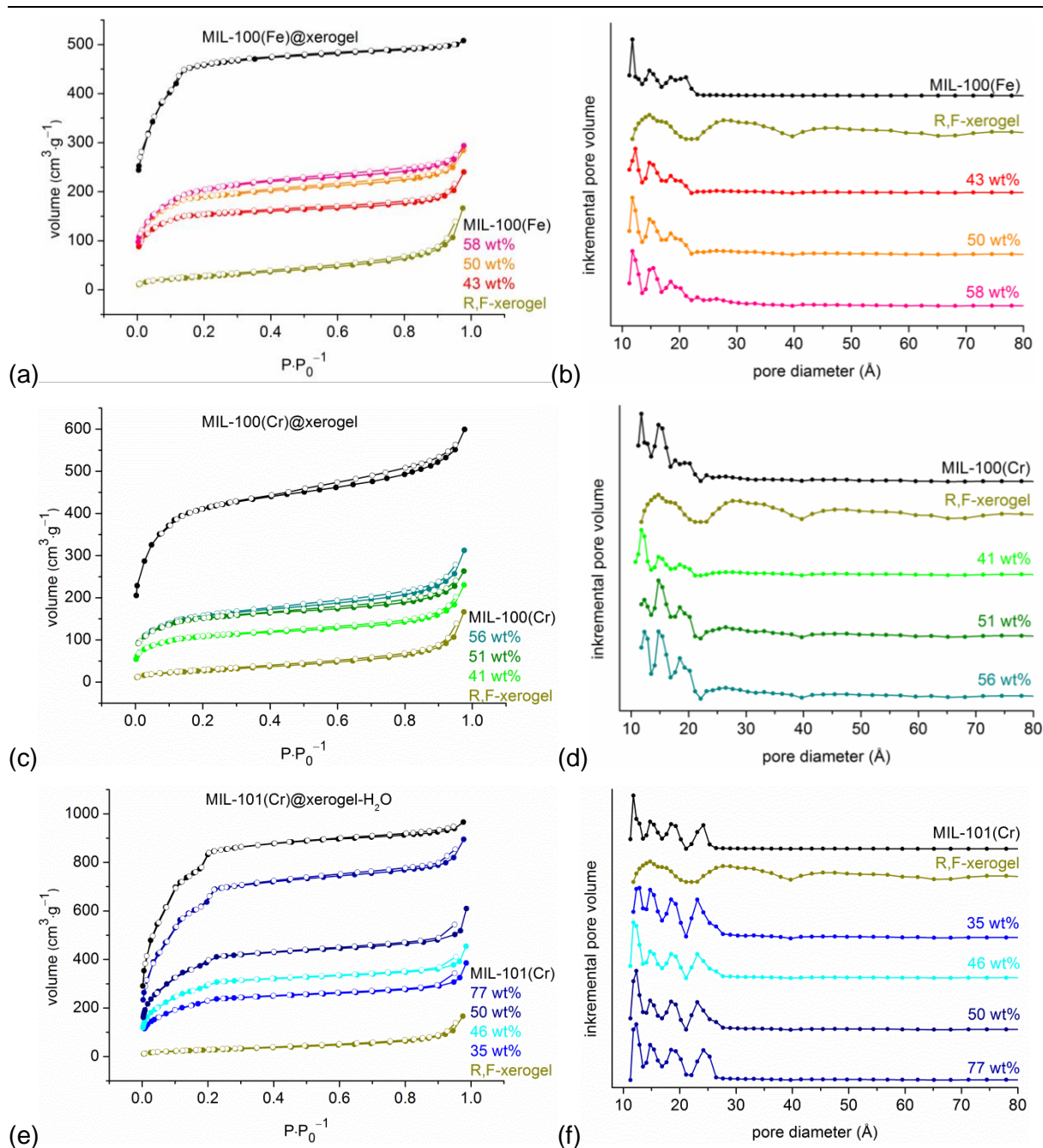
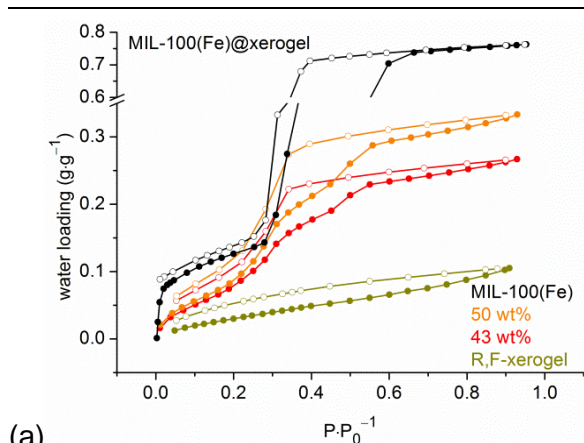
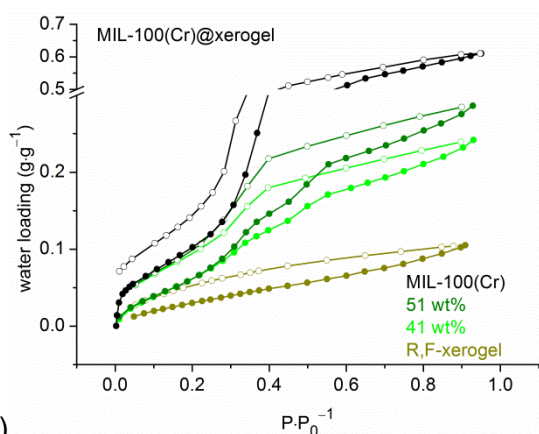


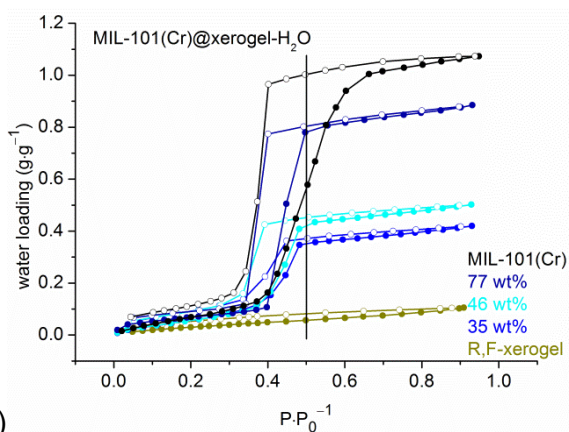
Fig. 7. N₂-sorption isotherms and pore diameter distribution of R,F-xerogel, MILs and MIL@xerogel composites. See Table 1 for BET surface areas and total pore volumes. (a,b) MIL-100Fe, (c,d) MIL-100Cr, (e,f) MIL-101Cr (a-d: MIL-100@xerogel; e,f: MIL-101(Cr)@xerogel-H₂O). For enlarged pore size distribution curve of bulk MILs see Fig. A.2c, A.4c, A.6c (degassing conditions: 3 h, 423 K). Adsorption is depicted with filled, desorption with empty symbols. N₂ sorption data of MIL-101(Cr)@xerogel without water addition is shown in Fig. A.13 (a,b).



(a)



(b)



(c)

Fig. 8. Water vapor sorption isotherms of R,F-xerogel, MILs and MIL@xerogel composites.

(a) MIL-100(Fe)@xerogel, (b) MIL-100(Cr)@xerogel, (c) MIL-101(Cr)@xerogel-H₂O (degassing conditions: 3 h, 423 K). Adsorption is depicted with filled, desorption with empty symbols.